2009-05

Pre-Stall Instability Distribution Over a Transonic Compressor Rotor

Gannon, A.J.

Journal of Fluids Engineering, Volume 131, May 2009.
http://hdl.handle.net/10945/44962

Pre-Stall Instability Distribution Over a Transonic Compressor Rotor

A. J. Gannon

G. V. Hobson

Turbopropulsion Laboratory,
Naval Postgraduate School,
Monterey, CA 93943

An investigation of the behavior of a transonic compressor rotor when operating close to stall is presented. The specific areas of interest are the behavior and location of low-frequency instabilities close to stall. In running close to stall, compressors can begin to exhibit nonperiodic flow between the blade passages even when appearing to be operating in a stable steady-state condition. The data from the current rotor clearly show that low-frequency instabilities were present during steady-state operation when stall was approached. These frequencies are not geometrically fixed to the rotor and typically appear at 0.3–0.8 of the rotor speed. The presence of these low-frequency instabilities is known and detection is reasonably commonplace; however, attempts to quantify the location and strength of these instabilities as stall is approached have proved difficult. In the current test fast response pressure sensors were positioned in the case-wall; upstream, downstream, and over the rotor blade tips. Simultaneous data from the sensors were taken at successive steady-state settings with each being closer to stall. A time domain analysis of the data investigates the magnitude of the instabilities and their transient effect on the relative inlet flow angle. The data are also presented in the frequency domain to show the development and distribution of the instabilities over the rotor as stall was approached. Initially the instabilities appeared within the rotor row and extended downstream but at operation closer to stall they began to protrude upstream as well. The greatest amplitude of the instabilities was within the blade row in the complex flow region that contains phenomena such as the tip-vortex/normal-shock interaction and the shock/boundary-layer interaction. In addition as stall is approached the growth of the instabilities is nonlinear and not confined to one frequency. [DOI: 10.1115/1.3112388]

Keywords: transonic compressor, near-stall operation, nonaxisymmetric flows

1 Introduction

It has been observed experimentally that during operation near stall in an axial flow fan or compressor rotor the flow can become nonperiodic between blade passages and low frequency; below once-per-revolution, instabilities in the flow field can be present. These instabilities have been measured and reported for the current test rotor [1]. Labels such as spike and modal instabilities have been used to describe them [2,3]. In some early studies the instabilities were detected when stall was imminent and it was thought that these may be a precursor event. More recent work has shown that this phenomenon can be present even in so called steady-state conditions when operating near to stall or surge [4,5]. In this work they are called "low-frequency instabilities" to avoid confusion with precursor, spike, and modal instabilities and with poststall rotating instabilities. While low-frequency instabilities usually indicate that the machine operates near to stall they do not necessarily indicate that stall is imminent. Experimental results indicate that the magnitude of these low-frequency instabilities is significant [1].

Understanding of these structures has significance in the design of compressors with regard to their stable operation near to stall. Simulations that force a periodic assumption may not accurately predict stall or surge points, either being optimistic or pessimistic making design optimization difficult. Close to stall this periodic assumption becomes less accurate and it appears that in order to properly model the flow field an unsteady simulation of the complete rotor needs to be performed. The instabilities that resulted in the rotor meant it experienced as much as a 2 deg change in the inlet flow angle near stall over a 5–10 revolution period [1].

This study aims to more accurately quantify and present the magnitude and frequency of these instabilities in a transonic rotor. To do this simultaneous results of a number of sensors are combined to show the distribution of the instabilities over the rotor. The frequency and distribution of the instabilities are shown at various operating points each successively closer to stall. The distributions are of interest as the region of greatest magnitude of the instabilities occurred in the complex flow region containing the tip-vortex shock interaction and shock boundary-layer interaction. In addition as stall was approached the low-frequency instabilities are detectable well upstream and downstream of the rotor.

The detection of these low-frequency instabilities required the use of high-speed pressure sensors and good signal processing techniques. It will be shown that the instabilities do not behave in either a linear fashion toward stall nor do they occur at predictable frequencies. In addition the magnitudes of the instabilities were significant, which resulted in observable changes in the bulk flow properties.

There may be many possible mechanisms for the production of these low-frequency instabilities. The fact that the present test case was a rotor-only machined blisk seemed to indicate that they were inherent in the flow without the need for external excitation. Further improvement to stall margin for stable operation of future compressors close to stall will demand better methods to simulate these low-frequency instabilities and better understanding of their causes and effects on machine operation.

Contributed by the Fluids Engineering Division of ASME for publication in the JOURNAL OF FLUIDS ENGINEERING. Manuscript received August 18, 2008; final manuscript received January 29, 2009; published online April 23, 2009. Assoc. Editor: Chunill Hah. Paper presented at the ASME Turbo Expo 2008: Land, Sea and Air (GT2008), Berlin, Germany, June 9–13, 2008.

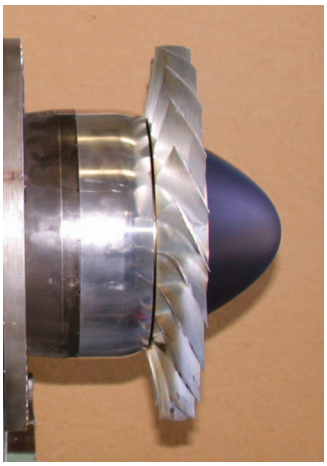

Fig. 1 Transonic test rotor

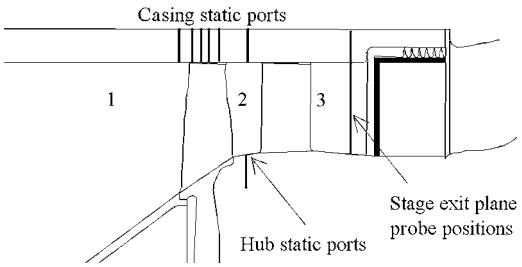

Fig. 2 Transonic test rotor

2 Experimental Apparatus

The rotor used, as shown in Fig. 1, was designed by Sanger [6] and subsequently tested by Gannon et al. [7]. A detailed description of the stage, instrumentation, and test rig, as well as methods to accurately determine the efficiencies, is contained in the papers [6,7]. To summate the rotor consisted of 22 blades of aspect ratio 1.2 with a design tip speed of 396.2 m/s (1300 ft/s), diameter of 0.2794 m (11 in.), and axial chord of 22.4 mm (0.884 in.). The rotor-only and stage design pressure ratios are 1.61 and 1.56, respectively, with a design mass flow rate of 7.75 kg/s (17.05 lb/s). The rotor was driven by an air turbine with the pressure ratio controlled by an upstream throttle.

2.1 Tip-Gap. An abradable strip was positioned over the rotor and before any runs took place the cold tip-gap was measured. Initially the machine was run to a particular low speed, shut down, and the new increased cold tip-gap measured. While this does cause a casing groove it ensures a small tip-gap. This process was repeated in steps until the design speed was reached. At 100% speed the rotor tip-gap was 25 μm (0.001 in.). This allowed the hot tip-gap to be inferred for different speeds as shown in Table 1.

2.2 Instrumentation. Two types of instrumentation, one set for steady-state performance measurement and a second for high-speed data capture, were installed on the rig. The steady-state instrumentation consisted of 2 upstream and 20 downstream Kiel stagnation-pressure probes. Stagnation-temperature probes to measure the efficiency consisted of two upstream and nine downstream [7]. An additional temperature sensor was embedded in a static port downstream of the rotor in the case-wall. The number of temperature probes has been increased from six to nine as this allows for more accurate efficiency measurement especially at off design conditions when the downstream temperature profile was distorted. The Kiel probe angles were also turned away from axial as no stator row was present. The angles were based on the streamline curvature code output from the design report of the rotor [8]. The angles are measured from axial, range from 45 deg at the hub to 39 deg at the tip. The stagnation Kiel probes used to measure the stagnation pressure have a high accuracy in the region of $\pm$54 deg in yaw and $\pm$49 deg in pitch. The probes were arranged at 15 deg intervals on a plane four axial chord lengths downstream of the rotor trailing tip as shown in Fig. 2.

The high-speed data system consisted of nine Kulite static-pressure transducers (referred to as high-speed sensors) over the rotor as shown in Fig. 3. Kulite sensors (1), (7), (8), and (9) were upstream of the rotor while sensor (2) was positioned at the leading edge and acted as the position reference. Sensors (3)–(5) were over the rotor and sensor (6) downstream of the rotor. One impact or stagnation Kulite sensor (10) was positioned upstream of the rotor facing the flow. It was positioned 0.44 of the rotor diameter upstream of the rotor at midspan (45 mm upstream of the nose cone) of the blade to measure the strength of the low-frequency instabilities upstream of the rotor. The sensors were sampled at 196.6 kHz giving 19.6 readings per blade passage at design speed. This was sufficiently high enough to ensure that the magnitude of any aliased higher frequencies was small.

3 Experimental Program

The present test program concentrated on compressor operation near to stall. The basic performance of the machine and the location of the stall lines were previously determined [7,9]. In addition the operating region for the appearance of the flow instabilities for the rotor-only case was known [1].

Detailed data at various speeds from the subsonic to the transonic region were taken. The compressor was not stalled at 100% speed in the rotor-only configuration due to concerns about the high overspeed during stall. For brevity, only the 70% speed, subsonic operation, and the 90% and 95% speeds, transonic operation are presented. Although the two transonic speeds are close the behavior of the low-frequency instabilities close to stall is markedly different.

To measure data for a particular speed line the compressor was set to operate in a steady-state condition at a point near to stall but far enough away that low-frequency instabilities were not expected to be significant. A sample of high-speed data was then taken. The compressor operating point was then moved incrementally closer to the stall point and data taken again. This allowed the development of these low frequencies to be observed as stall was approached. Data samples of 0.5 s were taken, which was sufficient to resolve the low frequencies of interest. At 95% speed this was equivalent to 214 rotor revolutions and approximately 100 cycles of the low-frequency flow variations.

Figure 4 shows the performance maps for the rotor-only configuration. Points at which the high-speed data were taken are shown with (A) being closest to stall and (F) farthest away. Point

Table 1 Rotor tip gaps

Speed (%)	70	90	95
Tip-gap	127 μm (0.005 in.)	25.4 μm (0.001 in.)	12.7 μm (0.0005 in.)
Tip-gap/blade chord	0.0025	0.0005	0.0002

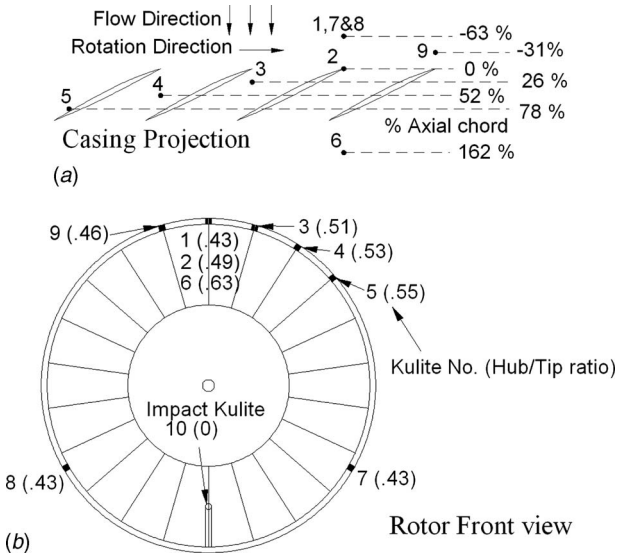

Fig. 3 Kulite sensor positions

(F) was at the full open throttle position of the test rig, point (E) was at peak efficiency, and point (D) was where low-frequency instabilities first appeared. These points are used for reference throughout the rest of the paper.

4 Postprocessing

4.1 Time Domain. In order to isolate the signals of interest in the time domain a selective filtering technique was required. These are well documented in the fields of signal processing but a basic outline found to be applicable to the current field is described here. A digital convolution filter method was used [10]. The steps are as follows: (1) A suitable filter was constructed in the time domain. (2) The sampled signal and filter are both transformed into the frequency domain using a fast Fourier transform (FFT). It was important to note that the FFT of the sampled signal and filter had to be of the same length. (3) A simple element by element complex multiplication of the filter and sample in the frequency domain was performed. (4) The product was converted back to the time domain using an inverse fast Fourier transform (IFFT) again of the same length to give the resultant filtered signal. The method for designing a low-pass digital filter was as

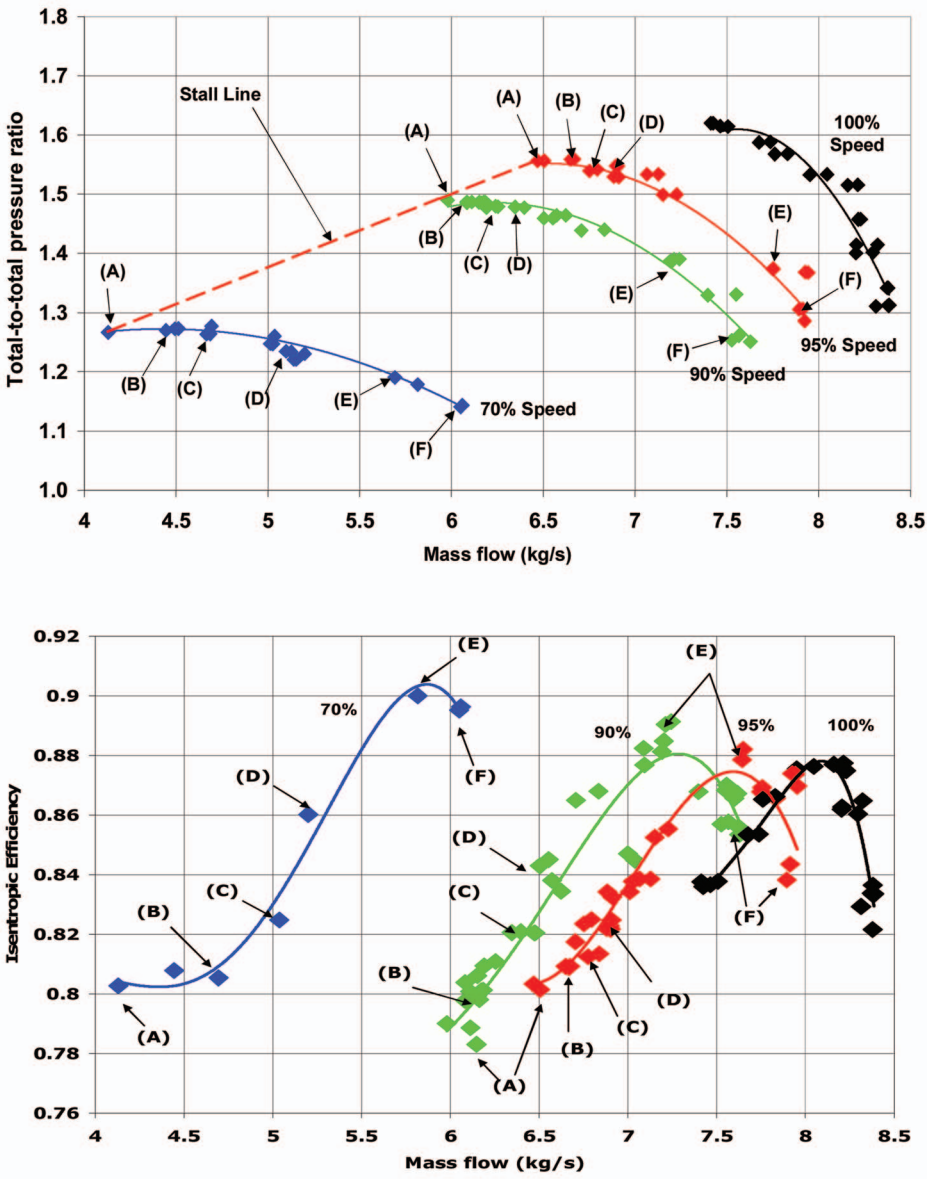

Fig. 4 Rotor-only performance maps

follows. The desired cutoff frequency f_c must be nondimensionalized by the sampling frequency

$$f_c = \frac{\text{cuttoff frequency}}{\text{sampling frequency}} \tag{1}$$

The roll-off bandwidth (BW) was defined as the desired frequency width where the signal dropped from 99% to 1% in strength. The constant BW was defined as follows

$$\text{BW} = \frac{\text{roll-off width}}{\text{sampling frequency}} \tag{2}$$

The bandwidth of the roll-off determined the number of points required for the digital filter and BW was used to construct a vector M from –2/BW to 2/BW in steps of 1 (2/BW must be rounded to an integer value)

$$M = -\frac{2}{\text{BW}}:1:\frac{2}{\text{BW}} \tag{3}$$

The so called sinc function was used to create an ideal low-pass filter vector h_{sinc} as follows

$$h_{\text{sinc}} = \frac{\sin(2\pi f_c M)}{2\pi f_c M} \tag{4}$$

Due to the filter length being finite a truncation error occurs that requires correction. To achieve this, a Blackman window is used (w_{Black}) and results in near unity gain in the band-pass region

$$w_{\text{Black}} = 0.42 - 0.5\cos\left(\frac{2\pi}{M}\right) + 0.08\cos\left(\frac{4\pi}{M}\right) \tag{5}$$

An element by element vector multiplication of the sinc filter h_c and Blackman window w_{Black} gave the filter shape h_{Black}. The filter must be normalized to ensure a unity gain in the pass region to get the final filter h as follows

$$h_{\text{Black}} = h_{\text{sinc}} \times w_{\text{Black}} \Rightarrow h = h_{\text{Black}}/\sum h_{\text{Black}} \tag{6}$$

To create a high-pass filter, all the elements of h_{Black} were multiplied by -1 and unity added to the central sample. A low-pass, h_1, and high-pass, h_2, filter were then combined to form a band-pass filter. Multiple band-pass filters can be added together but only one was used here. With the desired digital filters constructed the steps outlined earlier can be used to filter the sampled signal S to obtain the filtered signal S_f

$$S_f = \text{IFFT}(\text{FFT}(S) \times (\text{FFT}(h_1) \times \text{FFT}(h_2))) \tag{7}$$

MATLAB was used to perform the filtering techniques, which had built in functions to perform the above listed operations. All frequencies were normalized to the rotor speed in rpm. The band-pass frequency filter was from 0.3 to 0.85 with a roll-off of 0.05 rpm.

4.2 Frequency Domain. Observation of the signals in the frequency domain was also useful. In order to better isolate the low-frequency signals the signals were transformed into the frequency domain using FFTs as these were computationally cheap and easily implemented. A spectral analysis of the frequency data showed the magnitude and frequency of the sampled pressures over the rotor. The long data samples and high sampling rate ensured minimal aliasing and a good signal to noise ratio. To ensure that the correct magnitude of a particular frequency was captured the sampled signals were padded with zeros, usually eight times the length of the sample. Practically this was done by performing a longer FFT than the number of points in the sample. If this very simple method was not used the magnitude would often be cropped especially at lower frequencies [10], which were of special interest in this research.

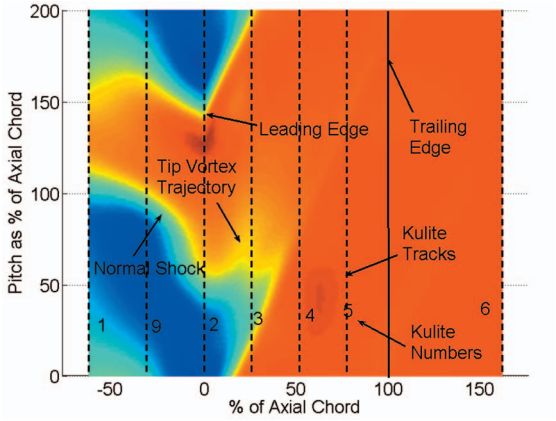

Fig. 5 Experimental pressure contours near stall, 95% speed (A)

5 Results

Figure 5 shows the experimentally obtained projection of the pressure contours by the rotor on the casing. Superimposed in this figure are the measurement locations of the Kulite sensors as the rotor passes over them. It was obtained using 0.5 s of data at 95% speed (214 rotations=4717 blade passages). A full set of these figures is presented in Ref. [11]. The sensor positions can be cross referenced with the low-speed frequency data presented in the figures that follow. In addition the detached shock typical of near-stall flow, as well as the track of the tip-vortex as it impinges on the shock, is indicated.

5.1 Time Domain. Observation of the filtered signals is useful in that is shows that their magnitude is not insignificant as compared with the raw signal. The three main regions of interest at near-stall operation are focused on the inlet just upstream of the rotor, the rear part of the blade where the large low-frequency instability magnitudes are found, and downstream of the blade as this would affect any following blade rows.

Figure 6 shows an example of a signal passed through a band-pass filter with a pass band of 0.25–0.9 of rotor revolution. The flow condition was at 95% speed at the closest stable operating point near to stall (point (A) Fig. 4). Results from three Kulite sensors, (1) upstream, (4) within the blade row, and (6) downstream are shown. Underlying the filtered signals are the raw data to give a visual comparison of the magnitudes. The data are presented for 50 rotor revolutions. A closer inspection of the raw signal would show that the blade passing frequency is dominant as expected.

It should be noted that if the flow was periodic in the blade-to-blade sense, the filtered signal would be constant. This is clearly not the case as shown in Fig. 6. Upstream of the rotor at sensor (1) the filtered signal was fairly small when compared with the raw signal, which was dominated by the blade passing frequency. Once inside the blade row at sensor (4) the magnitude of the instabilities increased while the blade passing amplitude decreases and the instabilities became an appreciable fraction of the pressure variations. Once the flow had exited the rotor the instabilities were still present and would affect downstream blade rows. In addition to wake effects variations in the bulk flow would affect downstream blade row performance. In Fig. 6, for sensor (6) downstream of the rotor, the effects of the underlying instabilities can be seen on the raw signal, which correspond to the underlying low-frequency instabilities. In a simulation where a periodic assumption is made these would not be captured.

Figure 7 presents only the filtered signals on a larger scale with the upstream impact-sensor included. It can be seen that there is an amplification of the signal from the upstream impact-sensor (10) to the over-rotor sensor (4) and a slight decrease downstream

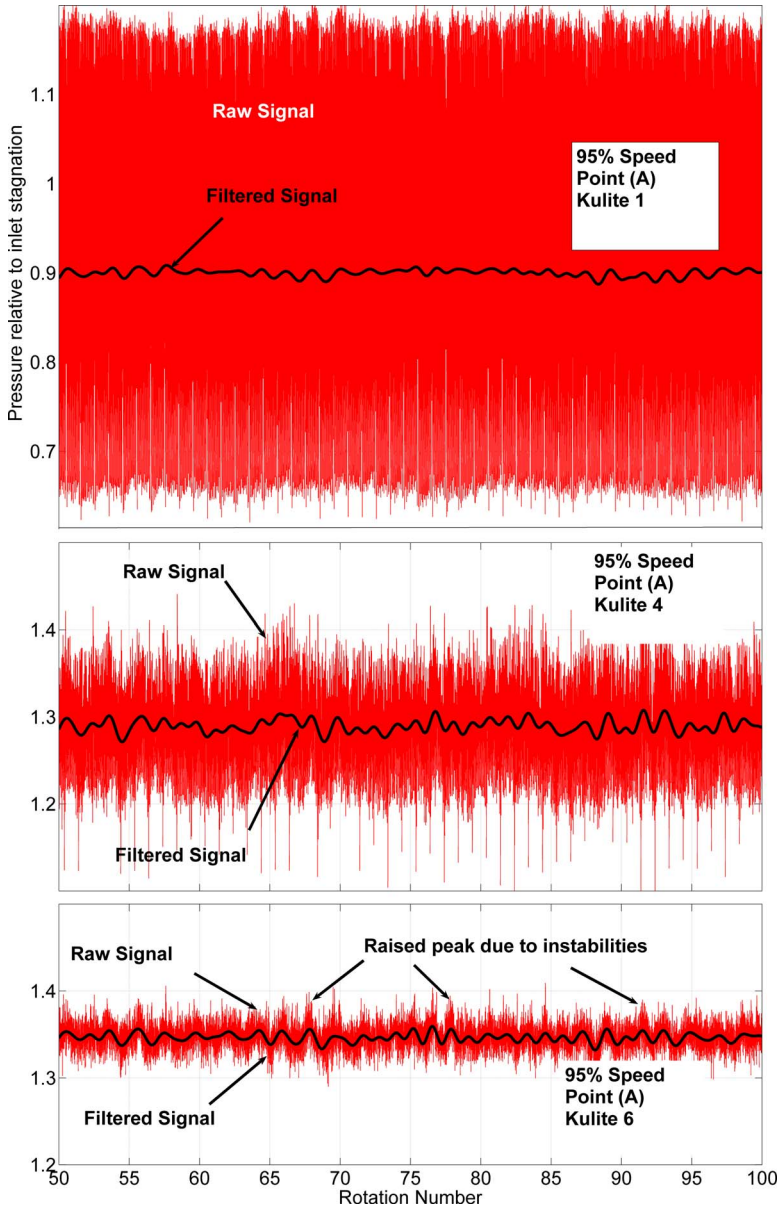

Fig. 6 Resultant filtered signal (95%)

of the rotor to sensor (6). These signals would be responsible for variations in the bulk flow not associated with the blade passing frequencies. The above signals were sampled simultaneously so it is also interesting to note that there are quite significant differences in the peaks. Where sensor (1) shows a small amplitude, sensor (4) shows a large one. The spectral analysis shows this in more detail.

Initial results looking at the variations of the inlet flow angle at 95% were presented by Gannon and Hobson [1]. Here too the assumption was made that the upstream stagnation pressure was constant. The amplitude of this filtered signal at the inlet is small when compared with the filtered static signal at the casing and assuming it is constant results in a more conservative calculation of the change in relative inlet angle.

Knowing the inlet static and stagnation pressures and using the measured upstream stagnation temperature allow the inlet Mach number to be calculated. Here the filtered signals derived from the Kulite sensors were used. In addition to the flow Mach number the blade tip speed was known and this allowed the low-frequency variation in the relative inlet angles to be calculated using a basic velocity triangle. Zero tangential inlet velocity was assumed but in the presence of changing circumferential static pressures such as those shown in Fig. 7 this was not strictly accurate. Figure 8 shows the variation in the rotor relative inlet angle for operation near to stall. In the figure the low frequency of the variations is evident with about 5 cycles for every ten rotor revolutions. A very low-frequency cycle was also observed at 95% speed but this was thought to be either a system oscillation or "beats" resulting from interference between the different frequencies.

Table 2 shows the amplitude of the variation for near 200 revolutions. The table shows that the effects of the low-frequency instabilities are significant. While it is not thought that the flow separates at the leading edge of the rotor blade, changes in inlet flow angle would affect the flow through the blade passage. As the frequencies of the instabilities are known we see that one peak-to-trough is roughly 0.75 of a revolution. Knowing the inlet speed we can then show through a rough calculation that the blade will have 14 chord lengths of flow from one peak-to-trough of a low-frequency signal. This would be sufficient time for the boundary

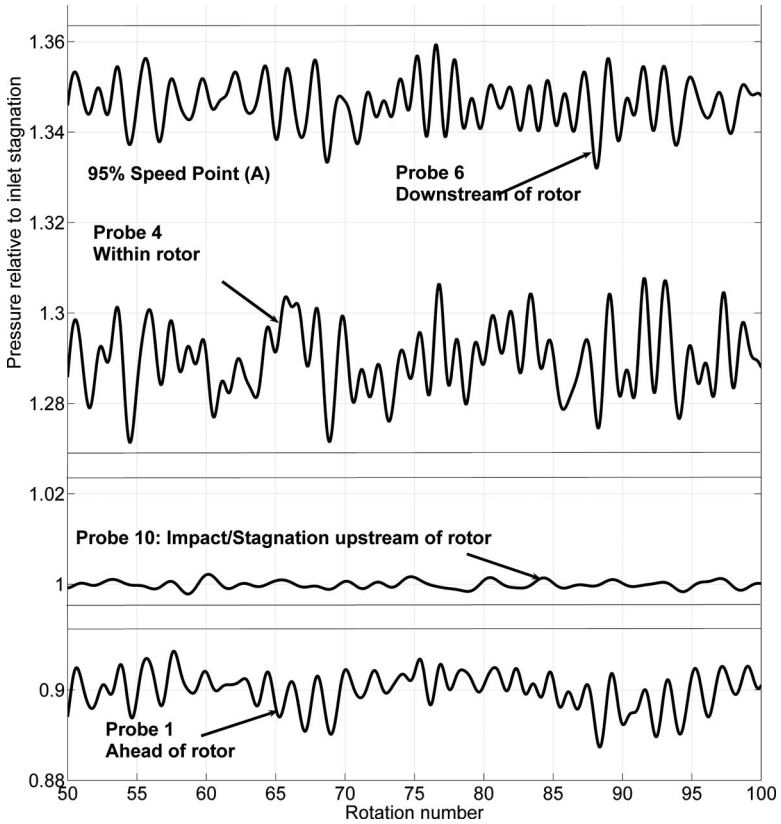

Fig. 7 Filtered signals through the rotor (95%)

layer to respond to these signals and thus each rotor passage would likely be operating along the relevant machine characteristic for a particular speed.

Tables 3–5 compare the peak-to-peak values of pressure for the raw unfiltered signal and the filtered signal for 95%, 90%, and 70% speeds, respectively, when operating close to stall. The tabulated 95% speed data correspond to those from Figs. 6 and 7. The filtered peak-to-peak values are a measure of the passage unsteadiness. At all speeds once the flow entered the blade row, the magnitudes of the low-frequency instabilities increased from the leading edge to the rear of the rotor. This is typical of diffuser type devices that tend to amplify flow distortions. This contrasted with the raw signal that was largest near the leading edge and decreased through the rotor thus increasing the ratio between the raw and filtered peak-to-peak amplitude through the rotor. The ratio of the peak-to-peak filtered over peak-to-peak raw data shown in the fifth column allows for comparison between speeds. This is most evident at probe (6) downstream of the rotor, which grows from 0.097 at 70% speed to 0.241 at 95% speed.

It is probable that it would be a peak and not a mean adverse pressure gradient that would precipitate a stall. The data in Tables 3–5 indicate that a downstream blade row may be subjected to a greater magnitude of instability than the one upstream of it. In the present rotor forcing periodicity would cause a simulation to fail to capture the nonaxisymmetry of the flow. It is thought that this would cause the greatest error in the prediction of the stability limit of the machine. Each individual passage would still be expected to operate along the unique characteristic of the machine.

5.2 Frequency Domain. A spectral analysis allowed for better observation of the distribution and magnitude of the low-frequency instabilities over the blade row. The spectral analyses were performed on the signals once they had been nondimensionalized to the inlet stagnation pressure (Figs. 6 and 7).

A brief summary of the method is shown in the following figures. Figure 9 shows the complete spectral power distribution from the single Kulite sensor (4) at 95% speed. The low-frequency region of interest below the once–per-revolution signal is indicated. The once-per-revolution signal was an indication of imperfections in the rotor. The largest magnitude was as expected at the blade passing frequency. Due to the high sampling speed a significant roll-off at high frequencies was found meaning that aliasing was minimal.

Figure 10 expands the low-frequency region presented in Fig. 9 on a linear scale. It shows the low-frequency instabilities that are present when operating close to stall. No clear higher-frequency harmonics of the signals were observed indicating that the instabilities are fairly pure sinusoidal signals. Recalling that the physical axial position of the Kulite sensors relative to the blade was known (Fig. 5) it is possible to present the distribution of the signals over the blades as shown in the next sets of figures.

Figure 11 shows the combined signals of the Kulite pressure sensors over the rotor presented as a waterfall plot. At each sensor position the relevant low-frequency spectrum similar to that shown in Fig. 10 is plotted. The four operating points presented correspond to those in Fig. 4 at 95% speed. All magnitudes from points (A) to (D) are plotted on the same vertical scale. A cursory observation of the figures indicates that there is a substantial change in the distribution and frequency of the low-frequency instabilities as stall is approached.

At point (D) small instabilities were present at the leading edge of the rotor row and decayed toward the trailing edge of the blade. At point (C), where the rotor was operating closer to stall, the first significant low-frequency instabilities occurred in the aft portion of the rotor at sensors (4) and (5). An inspection of Fig. 5 showed this to be behind where the normal-shock wave impinged on the blade suction surface. This region contains a thick boundary layer especially when operating close to stall. Moving even closer to stall to point (B) the dominant instability frequency abruptly

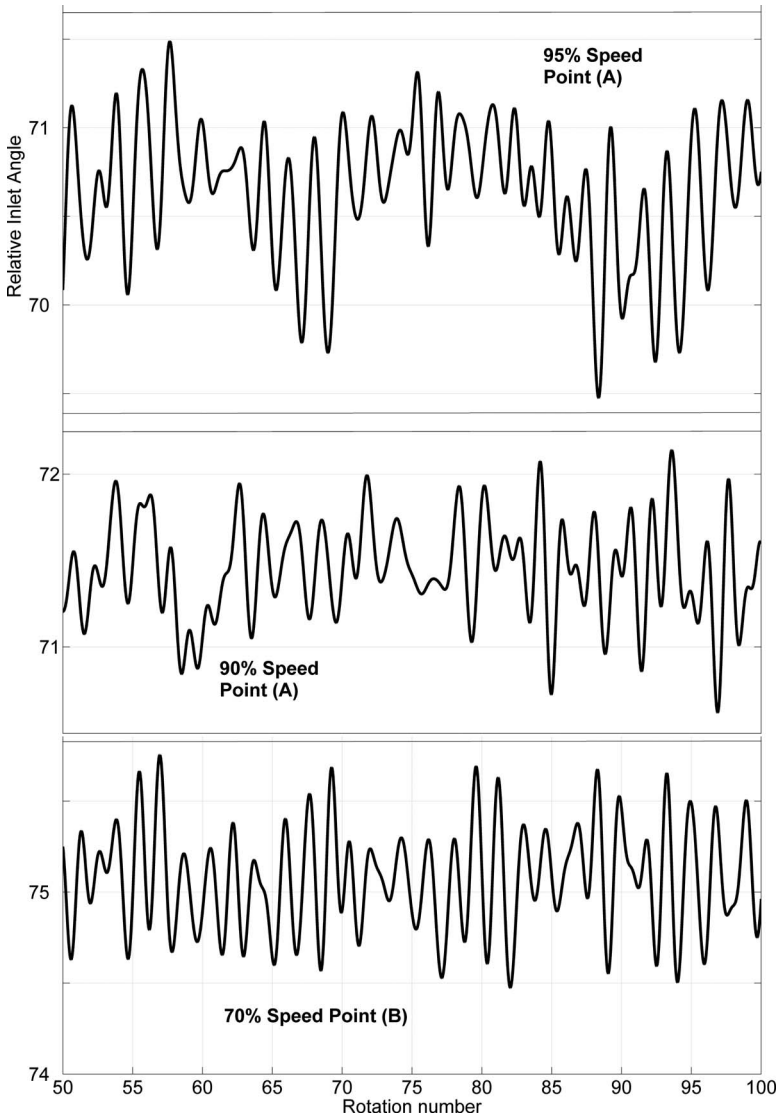

Fig. 8 Relative inlet angle variation close to stall

changed and in addition began to protrude ahead of the rotor blade. This could be due to the tip-vortex shock interaction becoming stronger and more complex. At point (A), the closest stable operating point before stall, one dominant frequency emerged. The position of greatest magnitude was found again at sensors (4) and (5) from midrotor to the trailing edge of the blade within the thick boundary-layer region. It could also be seen that

Table 2 Variation in inlet flow angle when operating near to stall

Speed and point	Mean inlet flow angle (deg)	rms variation (deg)	Peak-to-peak variation (deg)
95% (A)	70.6	0.351	2.04
90% (A)	71.5	0.341	2.21
70% (B)	75.1	0.269	1.65

Table 3 Variations in sensor pressure at 95% speed

Sensor No.	Mean pressure	Raw peak to peak	Filtered peak to peak	Ratio
10	1.00	0.094	0.0096	0.102
1	0.90	0.6069	0.0215	0.035
4	1.29	0.3767	0.0406	0.107
6	1.35	0.1453	0.0351	0.241

Table 4 Variations in sensor pressure at 90% speed

Sensor No.	Mean pressure	Raw peak to peak	Filtered peak to peak	Ratio
10	1.00	0.0502	0.0048	0.092
1	0.92	0.5649	0.0200	0.035
4	1.25	0.3281	0.0359	0.109
6	1.30	0.1269	0.0234	0.184

Table 5 Variations in sensor pressure at 70% speed

Sensor No.	Mean pressure	Raw peak to peak	Filtered peak to peak	Ratio
10	1.00	0.0335	0.0022	0.065
1	0.97	0.1426	0.0074	0.052
4	1.14	0.1826	0.0193	0.106
6	1.17	0.1029	0.0100	0.097

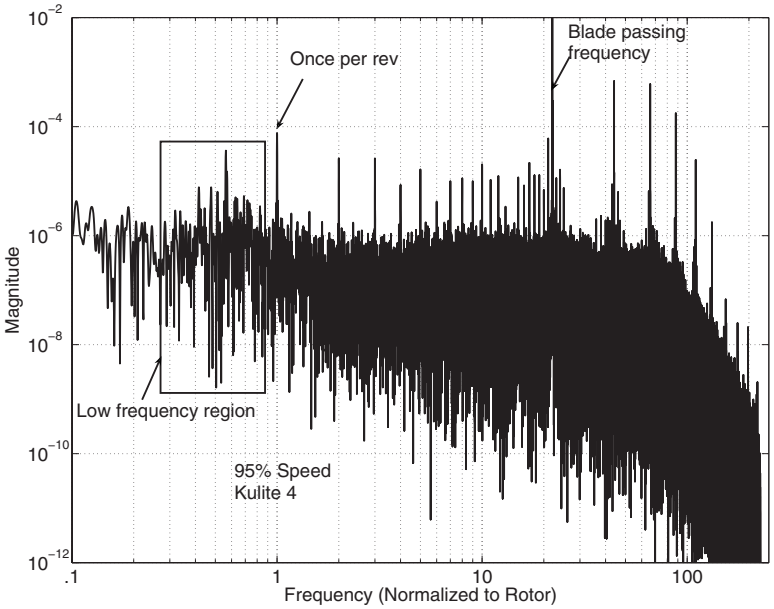

Fig. 9 Spectral analysis from FFT (log-log scale)

this instability was detectable upstream of the rotor in sensors (1) and (9) and as a small peak at the impact-sensor (10) more than five axial chords upstream.

For completeness Fig. 12 shows the low-frequency regions for peak efficiency and choked operation of the rotor at 95% speed. It can be seen that any low-frequency instabilities are barely detectable above the background noise. There was a slight increase in their strength as the compressor loading increased from a choked condition to peak efficiency.

Figure 13 presents the low-frequency instabilities for the 90% speed case again showing the four points closest to stall (Fig. 4). Again a constant vertical scale was used throughout the series of figures. The vertical scale is smaller than for 95% speed due to the lower speed. What was notable is that the relatively small difference in speeds caused a significantly different type of behavior in the instabilities as stall was approached. Point (D) was the first point where instabilities were significant. Operating slightly closer to stall at point (C) the magnitude of the instabilities increased. The largest magnitudes were again in the midchord region of the blade and a small instability was seen to protrude upstream. Moving closer to stall to point (B) four dominant frequencies began to emerge and the first significant signs of instabilities protruding upstream began to occur. As at 95% speed the largest region of instability was in the rear to trailing part of the blade and as stall was approached the instabilities did not decay behind the blade row. At point (A), the closest stable operating point to stall, two dominant instabilities emerged at 0.5 and 0.75 of rotor speed. The lower frequency protruded and was detectable well upstream of the blade row. The higher frequency had a larger magnitude but increased toward the rear of the blade row. Unlike at 95% speed, at 90% speed no single frequency emerged dominant suggesting that the mechanisms that cause these instabilities can act indepen-

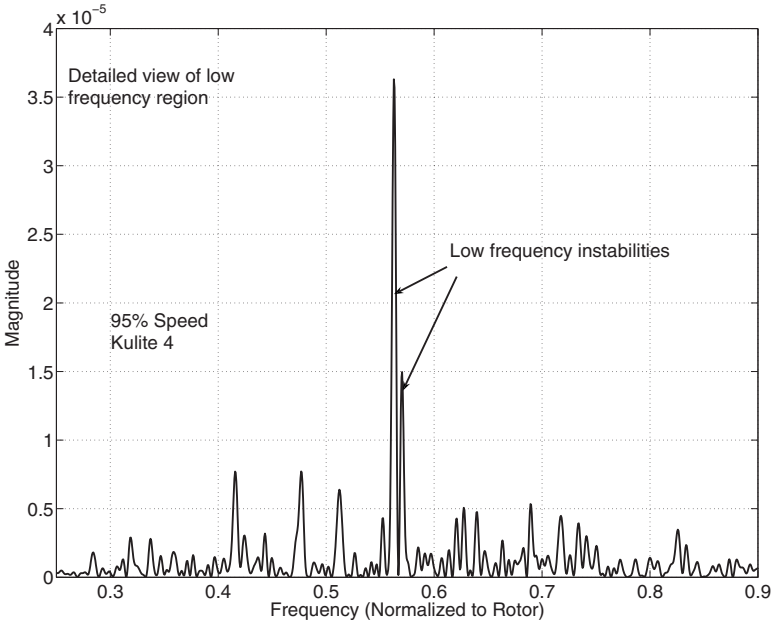

Fig. 10 Low-frequency region (linear scale)

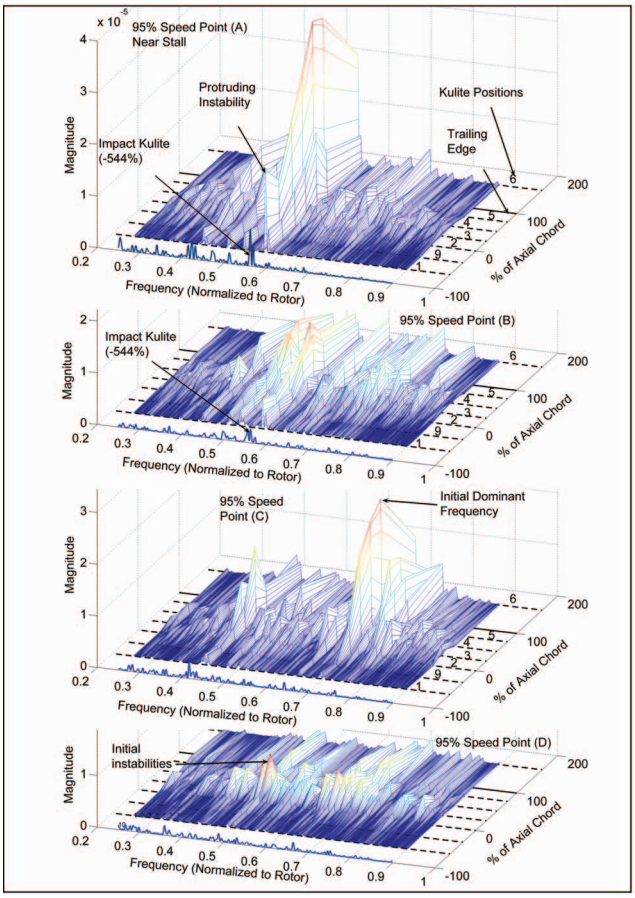

Fig. 11 Near-stall low-frequency instabilities (95%)

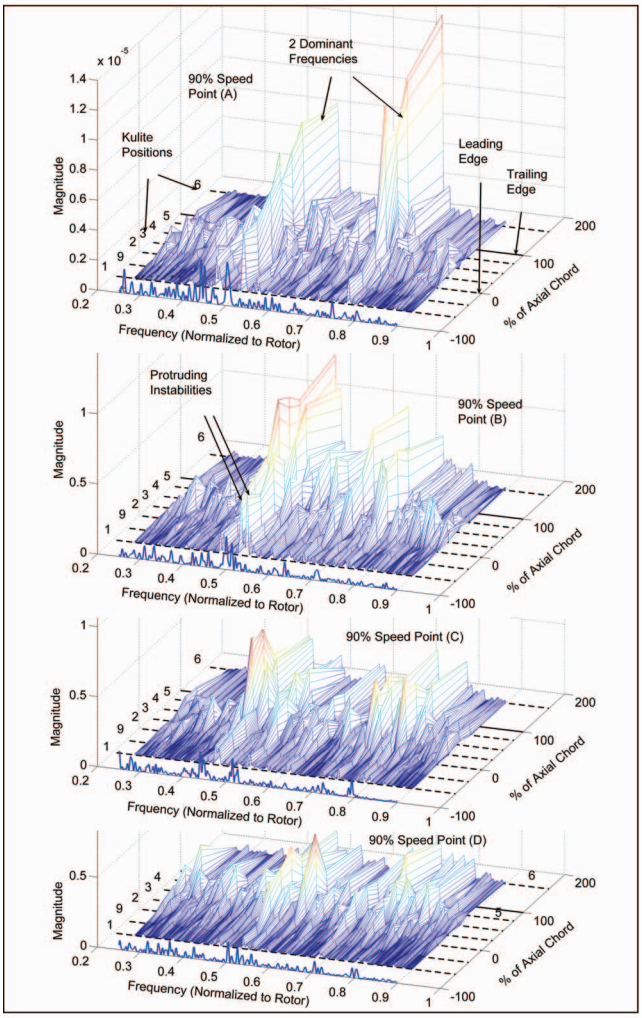

Fig. 13 Near-stall low-frequency instabilities (90%)

dently of each other.

Figure 14 shows the low-frequency instabilities for a subsonic case at 70% speed. The magnitude of the instabilities was lower at 70% speed but still detectable. Again a nonlinearity in the growth of the instabilities toward stall was present. At point (D) the instabilities first appeared and increased noticeably when approaching stall to point (C). Here two peak instabilities appeared, once again in the rear section of the blade passage. When moving closer to stall to point (B) more instability frequencies appeared but the peak magnitude was reduced. As with the transonic cases some instabilities protruded upstream of the rotor row.

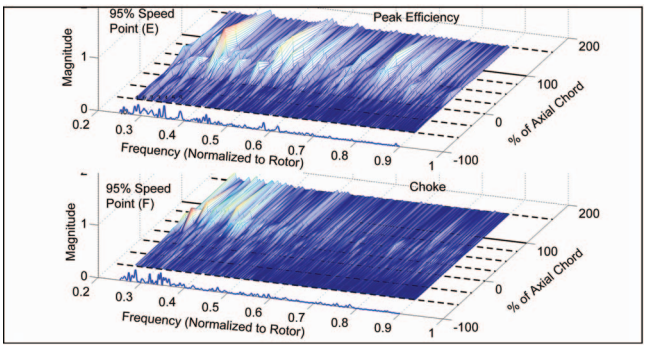

Fig. 12 Far from stall low frequencies (95%)

6 Discussion

The ability to observe the collective behavior of the low-frequency instabilities allowed some insight into their possible causes and the prestall characteristics of some transonic machines. It is important to recall that the periodic assumption of the flow in each passage being the same and steady relative to the blade does not always hold when operating close to stall [1,5]. Typical near-stall flow of a transonic machine contains a normal detached shock ahead of the blades with a tip-vortex that intersects the shock, which distorts it as shown in Fig. 5. The shock impinges on the suction surface of the blade ahead of it.

6.1 Protruding Instabilities. The so called protruding instabilities indicated in the previous figures were most likely due to the movement of the normal shock relative to the blade row as the shock clearly protruded upstream of the blade. At peak efficiency the shock in a transonic rotor is attached to the leading edge and thus geometrically fixed to the rotor. A detached normal shock would be affected by any change in the passage blockage and a changing position relative to the blade would have been detected upstream of the rotor. This movement may be due to multiple mechanisms as indicated by the more than one protruding-instability that were sometimes present (Fig. 13, (A) and (B)). The tip-vortex may also not be steady near stall and could affect the normal shock, which of course in turn would affect the following blade's flow.

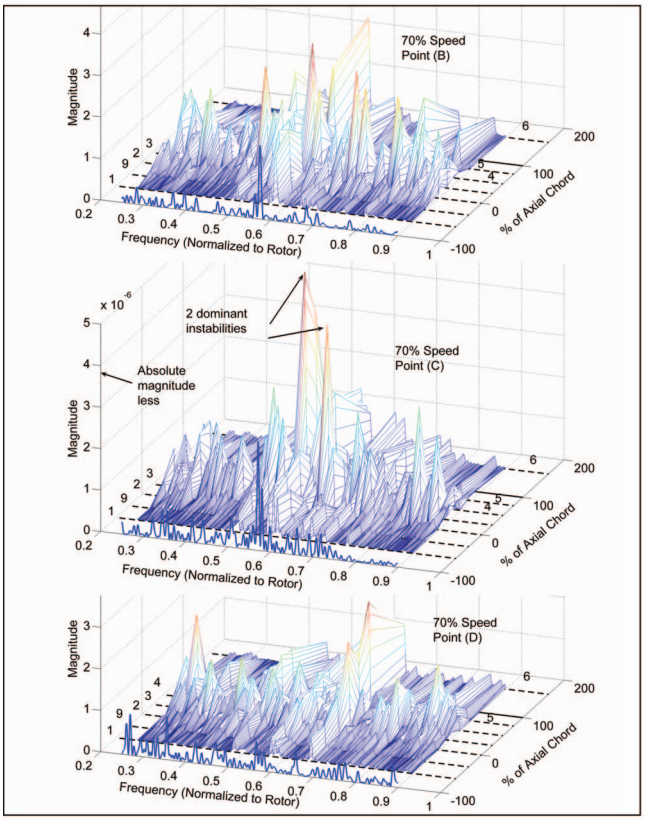

Fig. 14 Near-stall low-frequency instabilities (70%)

6.2 Peak Instability Region. The largest instabilities that appeared were within the blade passage at sensors (3)–(5) at all speeds. In this region the tip-vortex would have been interacting with the detached normal shock as mentioned before. This also corresponded axially to the location of the shock impinging on the blade suction surface. While the vortex-shock interaction has a strong influence in the tip region the shock-boundary impingement region occurs for a significant part of the span in a transonic machine especially at higher Mach number.

6.3 Instability Behavior. The behavior of the instabilities was generally nonlinear when approaching stall with different frequencies becoming dominant as stall was approached. It is important to note, however, that as long as they remain below a certain magnitude stall would not occur. The main difference between 95% and 90% speeds was that at 95% speed the two main instabilities coalesced. At 95% speed, one of the instabilities presumably acted as a strong forcing function causing the other to follow suit (Fig. 11). At 90% speed (Fig. 13) the two instabilities remained independent.

The exact mechanism that causes the instabilities can only be hypothesized here. They clearly moved relative to the rotor but only appeared when the compressor began to approach stall. The types of flow found in a rotor, such as the tip-vortex, its interaction with the shock, and the detached normal shock would vary with small disturbances in the external flow field. A variation due to a small disturbance in one passage would affect the flow in the following passage akin to a stall cell. This type of behavior could reinforce itself after a number of trips around the rotor and eventually lead to the larger detectable variations that were observed. As stall is approached the adverse pressure gradients increase and flows with adverse pressure gradients such as in diffusers and rotors tend to amplify flow disturbances.

6.4 Influence on Stall. It is thought that the eventual cause of stall in a transonic rotor is a region of separated flow that spreads and becomes large enough to cause a change in the operation of the compressor at a macroscale, usually detectable by a large reduction in the pressure ratio and mass flow rate. This distinction is important as rotors can operate with localized regions of separated flow with no adverse affects. The actual stall event itself is usually very rapid and develops in a stall cell within five to ten revolutions [4,9]. The low-frequency instabilities may cyclically increase the risk of a region of flow becoming a large scale separation.

6.5 Stall Prediction Improvements. The presence of instabilities, especially at multiple frequencies, makes the exact prediction of stall difficult. As noted it may take a number of revolutions of the machine for the conditions in the passage that cause a stall to be present. This may be different for each stall event. When simulating the flow making using of a periodic boundary assumption for the blade rows this in effect numerically damps out the low-frequency instabilities. Whether this makes the simulated prediction of stall pessimistic or optimistic depends on the machine. Ideally full rotor simulations are needed and the simulations will have to be conducted over many revolutions. If a full annulus, transient simulation was performed the shocks, tip-vortex, and boundary layers would be allowed to vary between passages. As was noted though the actual change in the flow of a single passage is quite slow, around 14 chord lengths peak-to-trough, which may leave some scope to using existing single passage steady-state methods to improve designs. A design change that would indicate a stall-margin improvement in a steady-state simulation is likely to lead to a stall-margin improvement in the real machine. However, if the low-frequency instabilities increased in magnitude as this study seems to indicate the magnitude of the improvement is likely to be less than predicted.

7 Conclusions

The distribution and magnitude of low-frequency instabilities in a transonic compressor rotor operating close to stall have been presented. Using effective sampling techniques, instrumentation, and appropriate numerical methods they can be isolated and observed. In isolating these low-frequency signals through the use of filtering techniques their magnitude in the time domain can be measured. It is shown that their magnitude was significant when compared with the dominant blade passing frequency. A spectral analysis of the instability region in the frequency domain was used to investigate the development and distribution of the instabilities over the rotor blade as stall was approached. Three different speeds, one in the subsonic and two in the transonic region, were investigated. The different behaviors served to demonstrate the unpredictable nature of the development of low-frequency instabilities. The instabilities were present upstream of the rotor and suspected to be due to the normal shock protruding ahead of the rotor and moving relative to the blade leading edge. The region of greatest magnitudes was found at midchord on the blade row, which contained the tip-vortex interacting with the detached normal shock and the normal shock impinging on the blade suction surface. The clear presence of these low-frequency instabilities means that the periodic boundary condition commonly used in simulations becomes less accurate as stall is approached. This could be one possible reason for the difficulty in predicting stall points with current methods.

Acknowledgment

The present study was part of the compressor research program sponsored by the Propulsion and Power Department of the Naval Air Warfare Centre, Patuxent River, MD with Ravi Ravindranath as the technical monitor.

References

[1] Gannon, A. J., and Hobson, G. V., 2007, "Pre-Stall Modal Instabilities in a Transonic Compressor Rotor," ISABE, Beijing, China.

[2] McDougall, N. M., Cumpsty, N. A., and Hynes, T. P., 1990, "Stall Inception in Axial Compressors," ASME J. Turbomach., **112**, pp. 116–125.

[3] Camp, T. R., and Day, I. J., 1997, "A Study of Spike and Modal Stall Phenomena in a Low-Speed Axial Compressor," ASME Turbo, Orlando, FL, Paper No. 97-GT-526.

[4] Bergner, J., Kinzel, M., Schiffer, H.-P., and Hah, C., 2006, "Short Length-Scale Rotating Stall Inception in a Transonic Axial Compressor: Experimental Investigation," ASME Turbo, Barcelona, Spain, Paper No. GT2006-90209.

[5] Hah, C., Bergner, J., and Schiffer, H. P., 2007, "Rotating Instability in a Transonic Compressor," ISABE, Beijing, China.

[6] Sanger, N. L., 1996, "Design of a Low Aspect Ratio Transonic Compressor Stage Using CFD Techniques," ASME J. Turbomach., **118**(3), pp. 479–491.

[7] Gannon, A. J., Hobson, G. V., and Shreeve, R. P., 2004, "A Transonic Compressor Stage Part 1: Experimental Results," ASME Turbo Expo, Vienna, Austria, Paper No. GT2004-53923.

[8] Sanger, N. L., 1999, "Design Methodology for the NPS Transonic Compressor," TPL Technical Note 99-01, Naval Postgraduate School, Monterey, CA.

[9] Gannon, A., Hobson, G., Shreeve, R., and Villescas, I., 2006, "Experimental Investigation During Stall and Surge in a Transonic Fan Stage and Rotor-Only Configuration," ASME Turbo, Barcelona, Spain, Paper No. GT2006-90925.

[10] Smith, S. W., 1997, *The Scientist & Engineer's Guide to Digital Signal Processing*, California Technical Publication.

[11] Gannon, A. J., Hobson, G. V., and Shreeve, R. P., 2005, "Measurement of the Unsteady Casewall Pressures Over the Rotor of a Transonic Fan and Comparison With Numerical Predictions," Paper No. ISABE-2005-1099.